A New Framework for X-ray Photon Correlation Spectroscopy Analysis from Polycrystalline Materials

Ronald M. Lewis III, ¹ Grayson L. Jackson, ² Michael J. Maher, ¹ Kyungtae Kim, ¹ Timothy P. Lodge, ^{1,3} Mahesh K. Mahanthappa, ¹ Suresh Narayanan, ⁴ and Frank S. Bates ^{1,*}

¹ Department of Chemical Engineering and Materials Science, University of Minnesota, Minneapolis, MN 55455, USA

²Department of Chemistry, University of Wisconsin-Madison, Madison, WI 53706, USA

³Department of Chemistry, University of Minnesota, Minneapolis, MN 55455, USA

⁴Advanced Photon Source, Argonne National Laboratory, Argonne, IL 60349, USA

*To whom correspondence should be addressed: bates001@umn.edu

ABSTRACT

We report a new analytical framework for interpreting data from X-ray photon correlation spectroscopy (XPCS) measurements on polycrystalline materials characterized by strong scattering intensity variations at fixed wavevector magnitude (*i.e.*, anisotropic scattering). Currently, no analytical method exists for the interpretation of the time-dependent anisotropic scattering from such materials. The framework is applied to interrogate the dynamics of a spherical micelle-forming diblock copolymer melt below the order-disorder transition, wherein finite size grains of micellar body-centered cubic structure produce anisotropic scattering. A wealth of analytical information is recovered from a simple measurement, including distributions of relaxation times and speeds associated with micelles within grains. The findings of this study demonstrate the efficacy of this new analytical method, which may be readily adapted for application to a variety of materials and systems.

I. INTRODUCTION

X-ray photon correlation spectroscopy (XPCS) in the small angle scattering geometry has become an established technique over the past two decades for studying the dynamics of liquid interfaces, 1 as well as many soft materials including colloids, 2,3 polymer thin films, 4 and polymer melts.⁵⁻⁷ The original implementation of XPCS used a point detector,⁸ which enabled dynamic measurements at a specific scattering vector \vec{q} ($|\vec{q}| = q = \frac{4\pi}{\lambda} \sin\left(\frac{\theta}{2}\right)$, where λ is the wavelength of the incident beam and θ is the scattering angle). However, advances in detector technology and data processing methods have enabled two-dimensional (2D) data acquisition over a wide range of \vec{q} . Thus far, small angle XPCS studies with a 2D detector have been focused on samples which produce powder-like, isotropic scattering patterns (i.e., the scattered intensity is invariant as a function of the azimuthal angle φ at fixed q, see Figure 1). Other modes of XPCS involving flow or shearing of a material have also been explored; however, these studies have been restricted to amorphous materials. 11,12 We are not aware of any analytical methods for XPCS data analysis for materials that produce anisotropic scattering patterns (i.e., φ -dependent scattering). The lack of such tools limits the application of XPCS to studies involving the dynamics of various classes of nanostructured materials.

In a conventional XPCS measurement, the 2D scattered X-ray intensity from a disordered or amorphous material is measured as a function of time. As detailed in Section III (*vide infra*), an intensity-intensity autocorrelation function may be calculated from the scattering of each pixel on the detector. Assuming that the sample dynamics are independent of φ , the time correlations from individual pixels are azimuthally averaged over a group of pixels with nominally the same magnitude of q, to yield a correlation function for that q. Fitting these correlation functions yields characteristic relaxation times (τ) as a function of q. Furthermore, an apparent diffusion

coefficient⁷ (or in some cases, an average velocity³) may then be extracted by regression analyses. Critically, this analysis relies on the isotropic nature of the scattering from the material under investigation and the assumption of φ -independent sample dynamics.

Scattering from ordered, nanostructured materials presents additional challenges in the analysis of XPCS data. Variations in observed azimuthal intensity of a 2D SAXS pattern may be associated with multiple dynamic processes that cannot simply be averaged together. For example, SAXS analyses of a block polymer sample exhibiting coexisting ordered (crystalline) grains and partially disordered ("liquid-like") regions reveal a superposition of Bragg peaks on top of weaker inter-micelle correlation length scattering at essentially the same principal wavevector magnitude q^* . While the XPCS signal from a single dynamic process may dominate, simple averaging of the data will convolve dynamic features from both crystalline grains and disordered liquid-like regions in the sample and lead to unreliable conclusions. However, it is computationally expensive and statistically unfavorable to consider the ~800,000 pixels (and associated correlation functions) per measurement individually. To this end, the purpose of this report is to address these challenges by establishing a reliable method for analysis of XPCS data from polycrystalline materials. A compositionally asymmetric diblock copolymer, which forms a micellar body-centered cubic (BCC) morphology below the order-disorder transition (ODT), is used as a model system for this purpose. A series of XPCS studies have been performed on diblock copolymers in the disordered^{7,13} and ordered^{5,6,14} states. However, the BCC morphology has yet to be investigated. Scattering from a finite number of relatively large BCC grains with distinct orientations within the illuminated sample volume offers an ideal platform for developing the XPCS analysis from polycrystalline samples. The methodology described here

yields dynamic information that could not have been otherwise extracted using traditional analytical approaches.

This paper is organized into the following sections: Section II describes the sample preparation and setup; Section III outlines the theory and equations utilized for data fitting; Section IV discusses the results of model experiments and the implementation of the polycrystalline analysis; and Section V furnishes the conclusions of this work and its implications.

II. SAMPLE AND EXPERIMENTAL SETUP

A compositionally asymmetric poly(styrene)-*block*-poly(1,4-butadiene) (PS-PB) diblock copolymer was synthesized using well-established anionic polymerization techniques¹⁵ with a number-average molecular weight $M_n = 29$ kDa, dispersity $D = M_w/M_n = 1.06$, and a PB volume fraction of $f_B = 0.20$. These molecular characteristics were determined using a combination of ¹H nuclear magnetic resonance spectroscopy and size exclusion chromatography. A small amount (< 1 % wt) of butylated hydroxytoluene (BHT) was added to the sample to minimize its degradation over the course of the XPCS measurement. Previous reports have established that this quantity of BHT does not significantly impact the phase behavior. ¹⁶ This PS-PB sample forms a BCC phase with a unit cell parameter a = 26 nm ($q^* = 0.34$ nm⁻¹) and $T_{ODT} = 153 \pm 1$ °C, as established by SAXS and dynamic mechanical thermal analysis (DMTA) experiments, respectively.

All scattering measurements were performed at the 8-ID-I beamline of the Advanced Photon Source at Argonne National Laboratory. A schematic of the experimental setup is provided in Figure 1; detailed descriptions of the beamline configuration and its modes of operation are provided elsewhere.¹⁷ A monochromatic, coherent incident beam with $\lambda = 1.14$ Å was utilized in this study. The polymer sample was loaded into a cylindrical fluid cell holder

which was 3 mm in diameter, 3 mm thick, and had stainless steel walls and polyimide (Kapton®) windows on each end. Prior to sealing the fluid cell, the PS-PB sample was annealed in the disordered state at T=170 °C for 2 minutes to equilibrate the material and remove air bubbles, which could give rise to artifacts. The beam size was trimmed and collimated to 20 μ m × 20 μ m and therefore the total illuminated sample volume was roughly 1.2×10^6 μ m³, which is sufficiently large to capture scattering from many distinct grains in the ordered state. The fluid cell was placed onto a copper block equipped with a Peltier cooler and a resistive heater for precise temperature control (\pm 0.1 °C). A relatively small fraction of the incident beam intensity (< 0.02 %) was scattered by the sample and collected on a LAMBDA 750K 2D pixel array detector, with a sample-to-detector distance of 4 m. The total collection time was 1000 s with a detector capture rate of 1 frame/s. Sample stability was assessed throughout the course of the measurement by monitoring the primary peak position and total scattered intensity as a function of time. We did not observe any significant variations in these metrics, consistent with sample stability during the experiment.

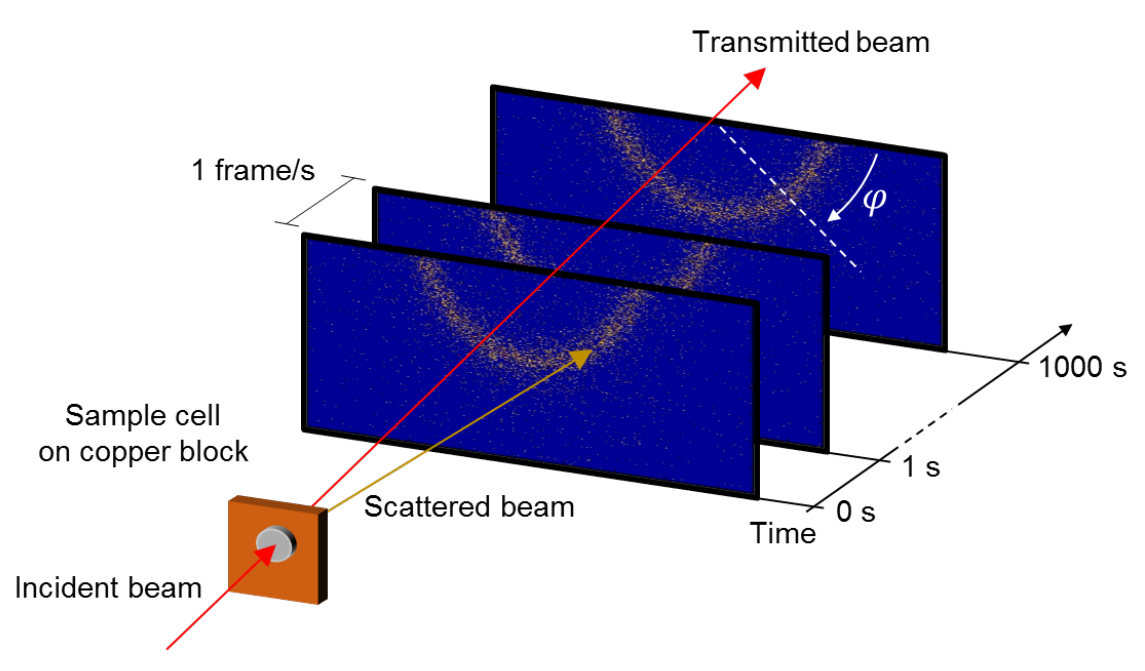


Figure 1: Experimental setup for XPCS measurements. The incident beam passes through the sample, which is held on a copper block with resistive heating and Peltier cooling capability. Scattered photons were collected at a rate of 1 frame/s for a total of 1000 s to enable calculation of the intensity-intensity auto-correlation function $g_2(q, dt)$.

III. THEORY AND FITTING MODELS

The normalized intensity-intensity autocorrelation function $g_2(q, dt)$ is defined as,

$$g_2(q,dt) = \frac{\langle I(q,t)I(q,t+dt)\rangle_t}{\langle I(q,t)\rangle_t^2},\tag{1}$$

where t is the time and dt is the time increment. Assuming that the scattered field is a Gaussian random variable, the intensity autocorrelation function is related to the intermediate scattering function $g_1(q, dt)$ according to the Siegert relation for homodyne scattering,

$$g_2(q, dt) - 1 = c|g_1(q, dt)|^2,$$
 (2)

where c is a sample-independent instrumental optical coherence parameter. Homodyne scattering corresponds to a single frequency among scattered photons, such that the scattered field is correlated with itself ('self-beating'). In the case of conventional homodyne XPCS, the

intermediate scattering function is characterized by a stretched exponential through the Kohlraush – Williams – Watts (KWW) equation,

$$g_1(q, dt) = \exp\left(-\left(\frac{dt}{\tau}\right)^{\beta}\right),$$
 (3)

where τ is the relaxation time and β is a stretching exponent. Ideally, the β parameter accounts for a distribution of relaxations and its magnitude enables discrimination between diffusive or non-diffusive behavior.^{3,20} If the dynamics of the material are governed by a single relaxation process, then $\beta = 1$ and the correlation function decays exponentially. Combining Equations 2 and 3 yields the relationship,

$$\frac{g_2(q,dt) - b}{c} = \exp\left(-2\left(\frac{dt}{\tau}\right)^{\beta}\right). \tag{4}$$

wherein b is a baseline value included for fitting purposes.

While the above analysis is typically appropriate for conventional XPCS analysis, we have observed a unique heterodyne scattering^{21,22} phenomenon with the block polymer BCC morphology, as described in Section IV. Heterodyne scattering is the consequence of mixing multiple scattered photons (due to the presence of multiple oscillators), each with a unique frequency.¹⁹ The effect of heterodyne scattering on the intermediate scattering function, which is described at length elsewhere,^{4,23} is briefly summarized as follows. If at least one component in the system within the coherently illuminated volume is in motion with velocity \vec{v} , then $g_1(\vec{q}, dt)$ is no longer described by Equation 3. Rather, for a material undergoing uniform motion with a single relaxation process the intermediate scattering function may be generally described by,

$$g_1(\vec{q}, dt) = \exp\left(i(\vec{q} \cdot \vec{v})dt - \left(\frac{dt}{\tau}\right)^{\beta}\right). \tag{5}$$

Note that insertion of this relationship into Equation 2 recovers the simple homodyne case (Equation 4) since all phase information is lost. However, if two separate scattering events occur, each with an independent relaxation time and velocity, the intensity-intensity autocorrelation function now becomes,

$$\frac{g_2(\vec{q}, dt) - 1}{c} = \left\{ X \left| g_{1,A}(\vec{q}, dt) \right|^2 + (1 - X) \left| g_{1,B}(\vec{q}, dt) \right|^2 + 2X(1 - X)Re \left[g_{1,A}(\vec{q}, dt) \cdot g_{1,B}^*(\vec{q}, dt) \right] \right\}$$
(6)

where A and B correspond to the two uniquely scattering populations and X quantifies the scattering intensity contribution from process A relative to the total scattered intensity,

$$X = \frac{I_A}{I_A + I_B}. (7)$$

Considering two separate processes, implementing the expression of $g_1(\vec{q}, dt)$ given by Equation 5 into Equation 6 leads to the symmetric heterodyne relationship,

$$\frac{g_2(\vec{q}, dt) - b}{c} = \left\{ X \exp\left(-2\left(\frac{dt}{\tau_A}\right)^{\beta_A}\right) + (1 - X) \exp\left(-2\left(\frac{dt}{\tau_B}\right)^{\beta_B}\right) + \\
+2X(1 - X) \exp\left(-\left(\frac{dt}{\tau_A}\right)^{\beta_A} - \left(\frac{dt}{\tau_B}\right)^{\beta_B}\right) \cos\left[\left((\vec{q} \cdot \vec{v}_A) - (\vec{q} \cdot \vec{v}_B)\right) dt\right] \right\}. \tag{8}$$

The dot product of the wavevector and the velocity may be reduced to,

$$\vec{q} \cdot \vec{v}_i = q |\vec{v}_i| \cos(\varphi) = q u_i = \frac{\omega_i}{2\pi},\tag{9}$$

where u_i is an apparent speed and ω_i is an apparent frequency of process i = A or B. Substitution of Equation 9 into Equation 8 yields,

$$\frac{g_2(dt) - b}{c} = \left\{ X \exp\left(-2\left(\frac{dt}{\tau_A}\right)^{\beta_A}\right) + (1 - X) \exp\left(-2\left(\frac{dt}{\tau_B}\right)^{\beta_B}\right) + \right\}$$

$$2X(1-X)\exp\left(-\left(\frac{dt}{\tau_A}\right)^{\beta_A} - \left(\frac{dt}{\tau_B}\right)^{\beta_B}\right)\cos\left[\frac{\omega}{2\pi}dt\right],\tag{10}$$

where $\omega = \omega_A - \omega_B$ is the difference in frequency between the dynamic processes; here again, the parameter b has been included for fitting purposes. An important limiting case emerges from the heterodyne relationship described by Equation 10. If the relaxation times (τ_i) for the dynamic processes tend to infinity, the relationship simplifies to,

$$\frac{g_2(dt) - b}{c} = \cos\left[\frac{\omega}{2\pi}(dt - dt_0)\right],\tag{11}$$

where dt_0 is a fitting parameter that captures the arbitrary phase shift in the correlation function. These equations are utilized in the following section to classify the correlation functions measured with the PS-PB diblock copolymer in this study.

IV. EXPERIMENTAL RESULTS AND ANALYSIS

Nucleation and growth of the micellar BCC phase in this PS-PB diblock polymer sample was characterized in detail using dynamic mechanical spectroscopy (DMS) following procedures outlined elsewhere. In order to target a polycrystalline or "grainy" sample for XPCS analysis, the sample was cooled rapidly over ~ 2 minutes from the disordered state at 170 °C to 140 °C and annealed for approximately 7.5 h; time-temperature transformation (TTT) analysis based on DMS experiments revealed 100 % conversion to the BCC phase in less than 3 h following this protocol. Subsequently, 2D SAXS patterns were recorded for 1000 s at a rate of 1 frame/s. Figure 2A shows the final time-averaged 2D SAXS pattern, which is characterized by a narrow ring of highly anisotropic scattering intensity as a function of azimuthal angle φ at q^* (evident in the inset to Figure 2A). This non-uniform scattering intensity arises from the finite number of grains probed within the illuminated sample volume. Discrete higher-order diffraction spots, clearly evident at $\sqrt{2}q^*$, reinforce the morphological assignment. The 2D SAXS pattern was

azimuthally averaged to generate the one-dimensional result shown in Figure 2B, with arrows corresponding to the Bragg reflections associated with a BCC morphology. For the purpose of demonstrating the new analytical method, only dynamic processes in the vicinity of q^* were considered in this study. From the raw 2D data, each pixel at $q^* = 0.034 \pm 0.001$ Å⁻¹ was linearly correlated through time to generate the intensity-intensity autocorrelation function $g_2(q^*, dt)$. For simple systems exhibiting a single type of relaxation, a multi-tau^{26,27} method may be more suitable for determining $g_2(\vec{q}, dt)$. However, here we employ a linear correlation method, which is justified based on the heterodyne phenomenon reported later in this study. Although the experiment was performed for 1000 s, only the first 800 s of the correlation functions were utilized for analysis due to poor long delay statistics from the linear correlation method.

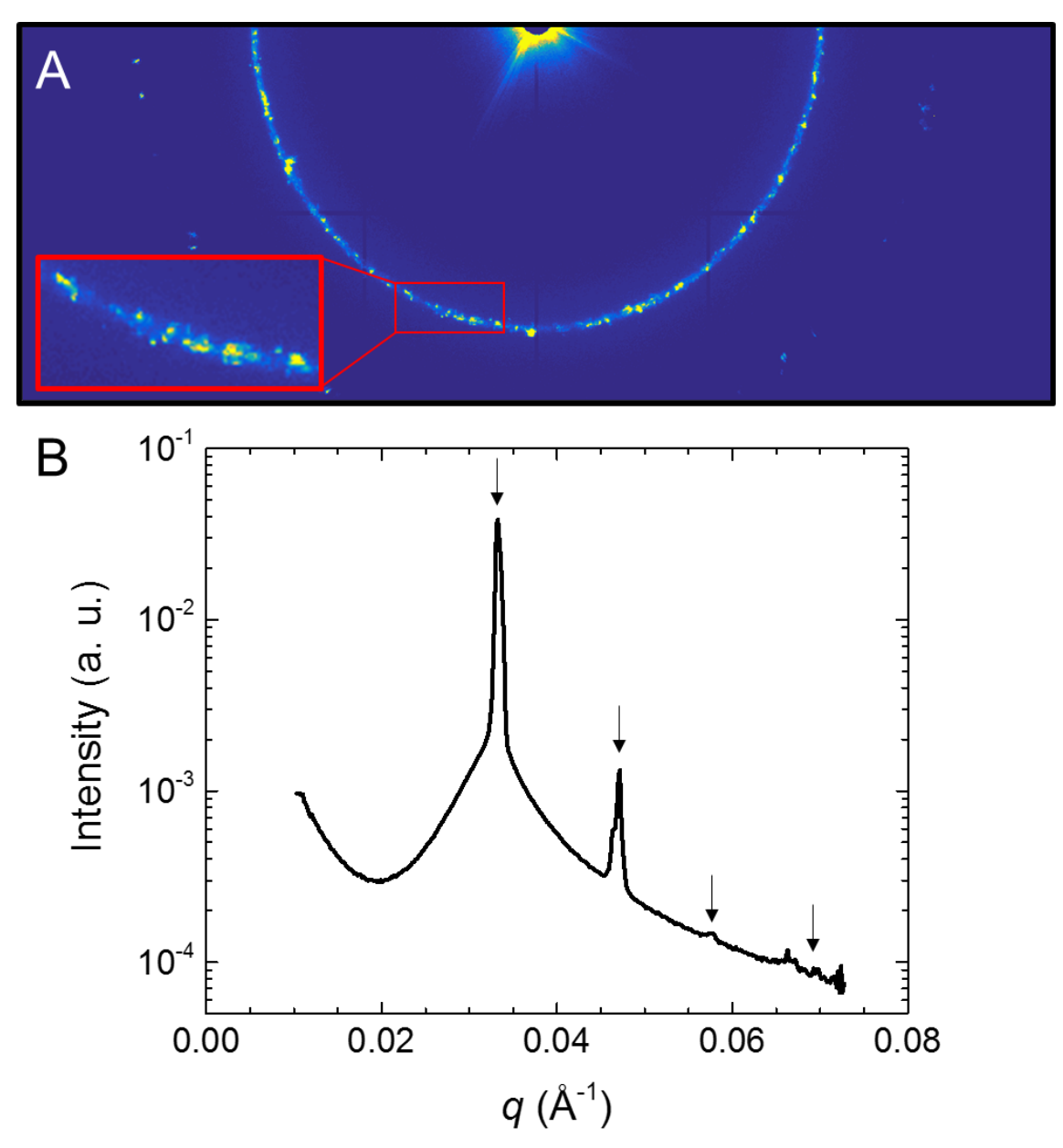


Figure 2: Time-averaged scattering from the PS-PB diblock copolymer after annealing at 140 °C for 7.5 h. (A) The 2D SAXS pattern reveals pronounced polycrystallinity as evidenced by the highly anisotropic intensities at the Bragg conditions, which are highlighted in the inset. The XPCS beamline geometry at sector 8-ID-I restricted our accessible φ -range to 180°. The 2D pattern in (A) was azimuthally averaged to produce the SAXS intensity profile shown in (B). The Bragg conditions are indicated by arrows and correspond to BCC reflections $((q/q^*)^2 = 1, 2, 3, 4, ...)$.

It is evident that simply averaging all correlation functions near q^* could lead to the convolution of many dynamic processes resulting in improper analysis (see Fig. S1). On the

other hand, with \sim 16,000 correlation functions (pixels near q^*) per measurement, it is impractical to consider each pixel individually. Therefore, a new φ mapping procedure was developed to balance resolution against statistics for scattering from the polydomain sample (Figure 3). First, the q^* region was split into 150 rectangular bins of roughly 100 pixels each, such that each bin center was offset by approximately 1.2° and spanned $\Delta q = 0.001 \text{ Å}^{-1}$ (rectangular bins were chosen for ease of analysis and resulted in the loss of ≤ 2 pixels per bin). While this number of bins provided the appropriate balance of statistics and resolution for this material, these parameters may be easily tailored for different experimental systems. As previously mentioned, the intensity of each pixel in the vicinity of q^* was linearly correlated through time. Within each of the newly created bins, the ~100 correlation functions were averaged to generate one correlation function per bin. The map was then rotated by $\Delta \varphi = 0.2^{\circ}$, and the correlation functions of each pixel were averaged again within the new bins. This process was repeated 5 times, such that the sixth rotated mapping of bins was identical to the first. As shown in Figure 3, superposition of the 5 rotated maps of bins onto the 2D image in Figure 2A yielded 750 total correlation functions at q^* . This mapping procedure enables high resolution and meaningful statistics without significant computational effort. We emphasize again that this process may be generalized to accommodate any polycrystalline sample by simply altering Δq , $\Delta \varphi$, and the number of bins (or the angle between bins).

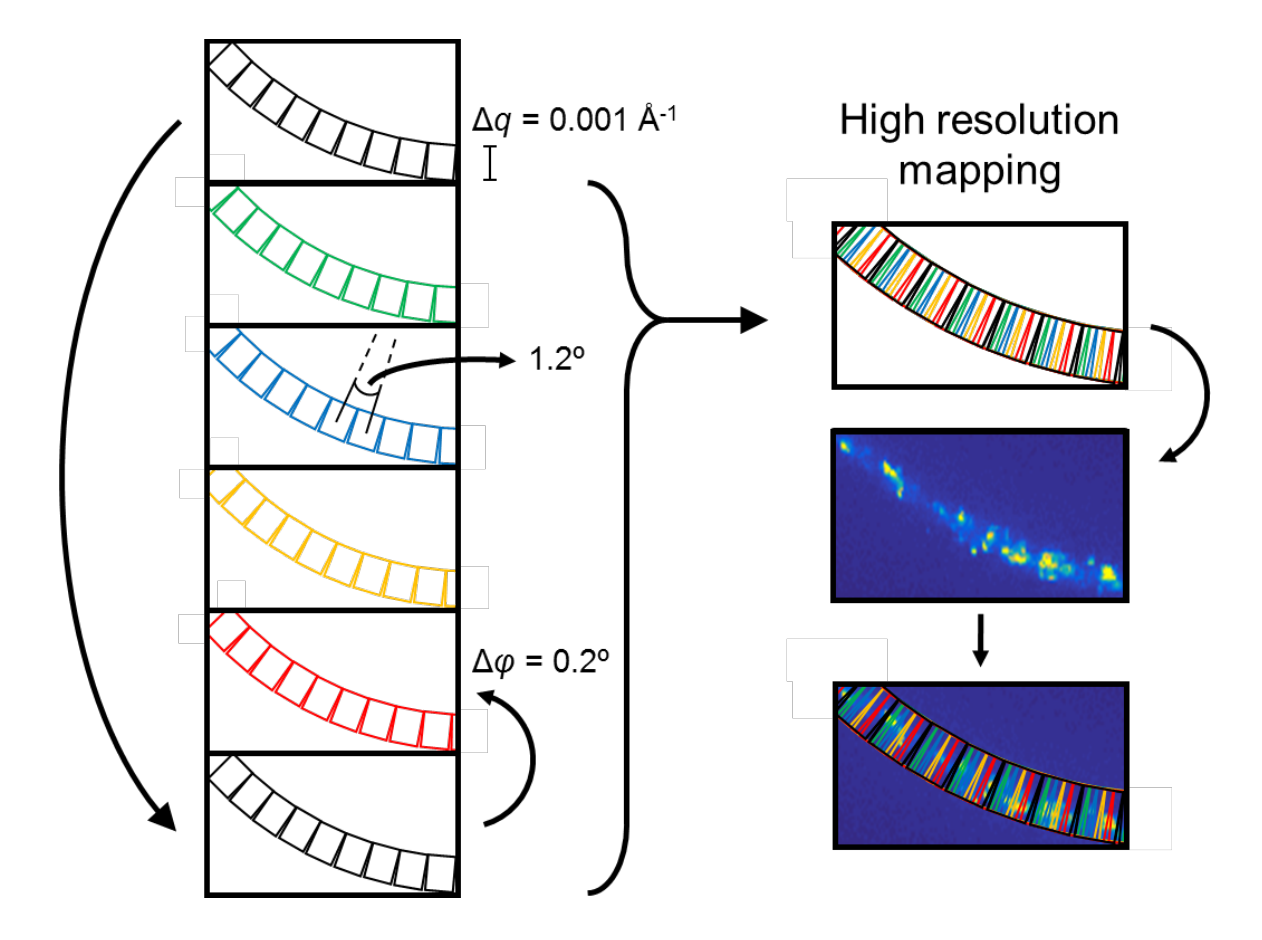


Figure 3: Azimuthal mapping procedure that was developed for polycrystalline scattering offering a balance between resolution and statistics. In this study, 5 rotated maps of 150 bins each were superposed and each bin was individually analyzed. The superposed bins were applied to the 2D images in the q^* region for analysis. This method can be generalized to accommodate any polycrystalline system by altering Δq , $\Delta \varphi$, and the number of bins.

After generating all 750 correlation functions, a rigorous and semi-automated procedure was developed to classify and, in some cases, fit each correlation. This procedure is outlined as a flow diagram in Figure 4A, while Figure 4B provides representative correlation functions for the final categories outlined in Figure 4A. Note that the fitting procedure described here is specific to the data from this experiment; nevertheless this fitting process may be adapted or generalized to analyze other systems. First, a single-sided fast Fourier transform (FFT) was performed on each correlation function to recast the correlation function into the frequency domain (f_s). In order to quickly categorize the bins, a linear regression (with fixed intercept at 0) of the FFTs integrated

with respect to f_s was utilized to quantify the level of noise in the data via the fitted R^2 value. The integrated FFT of a correlation function comprising random fluctuations about a mean value is a straight line with intercept at the origin. Therefore, bins with $R^2 \ge 0.9$ had a low signal-tonoise ratio and were considered to contain only very weak intensity pixels that did not satisfy the Bragg condition, which we refer to as off-grain (Figure S2). A bin with $0.5 < R^2 < 0.9$ was classified as either the result of a weakly scattering grain or an artifact of averaging pixels which contained Bragg and non-Bragg scattering. Bins with $R^2 \le 0.5$ had a high signal-to-noise ratio, and qualified for fitting (Figure S3). If the FFT exhibited a dominant peak that was not at the lowest frequency position ($\omega > 2\pi/(800 \text{ s}) = 0.00785 \text{ s}^{-1}$), an apparent frequency was present and the correlation function was fit with Equation 10 using τ_A , τ_B , and ω as fitting parameters to extract a more accurate frequency and the associated relaxation times (τ_A and τ_B). If this fit was successful based on the fit residuals and visual inspection, the correlation function was classified as a clean heterodyne and a frequency was extracted. Failure to fit to Equation 10 implied that the heterodyne scattering had a more complex origin, likely owing to the interference of more than two independent scatterers. For these complex heterodyne cases, speeds were estimated based on the dominant frequencies obtained from the FFT analysis.

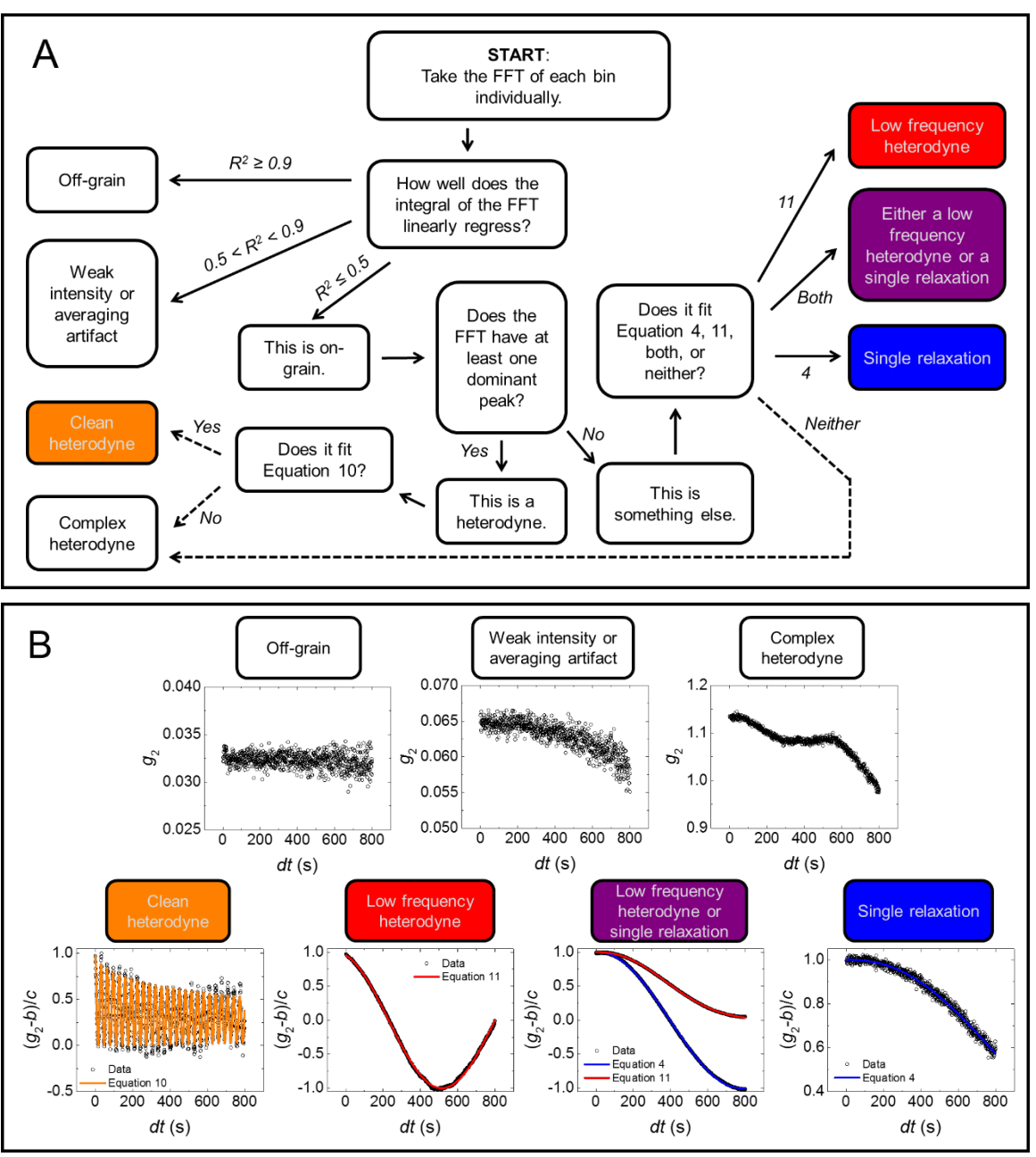


Figure 4: Classification and fitting scheme for each XPCS data bin in this study. The flow diagram in (A) categorizes the bins based on the single-sided FFT and fits of the correlation functions. Solid arrows indicate steps that were automated, and dashed arrows indicated steps that required manual user input. Representative datasets for each of the final bins are provided in (B), with data fits overlaid where appropriate.

If the FFT of a correlation function did not contain a dominant peak, it was fit using both Equations 4 and 11 and assigned to either Equation 4 (single relaxation), Equation 11 (low frequency heterodyne), both, or neither based on the residuals to the fit. In this study, fits were

considered successful if the sum of squared residuals for the scaled fit was < 2; this fitting criterion was chosen based on visual examination of the fits. In the rare case when neither Equation 4 nor Equation 11 fit the correlation function well (< 1 % of bins), the bin was classified as a complex heterodyne and was visually inspected to confirm this classification. The semi-automated nature of this fitting algorithm provides accuracy while minimizing the time required for analysis. Where applicable, examples of the described fits are displayed along with the datasets in Figure 4B. The clean heterodyne data and fit have been enlarged in Figure 5 for clarity. Figure 6 contains a stacked histogram showing the classification of all 750 correlation functions present in this study. We note that correlations from adjacent bins often resemble one another due to the large overlap of averaged areas. Despite this overlap, the different classifications of bins in Figure 6 originate from a variety of azimuthal angles.

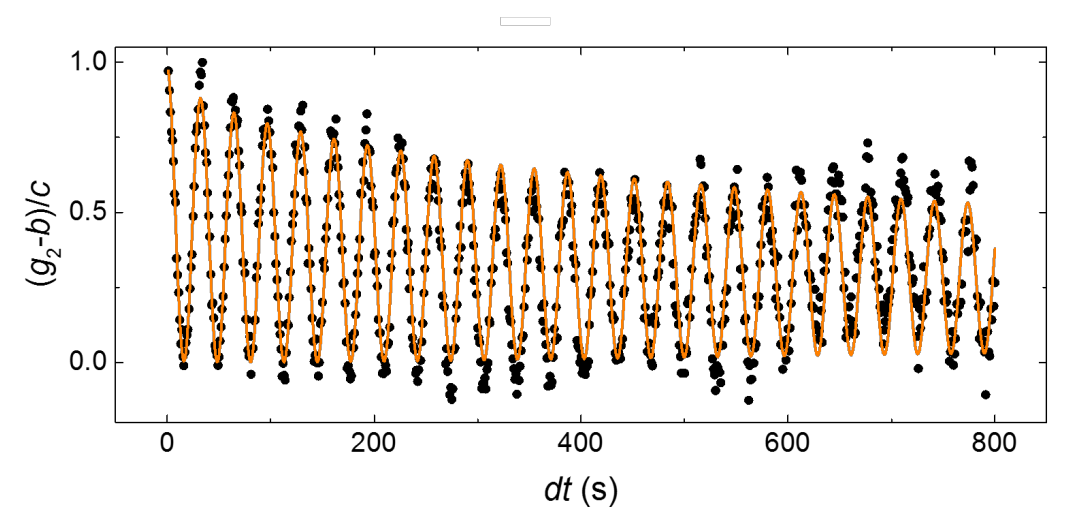


Figure 5: Representative clean heterodyne data and fit according to Equation 10. Despite fluctuations in the oscillation amplitude, a frequency can be extracted and converted into an apparent speed *via* Equation 9.

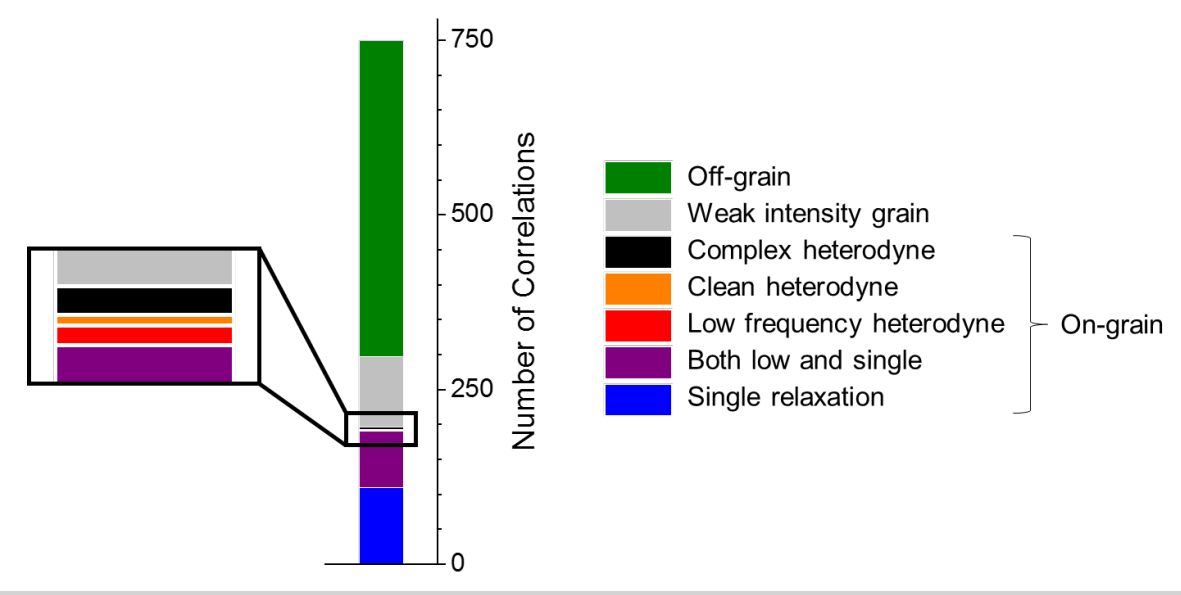


Figure 6: Stacked histogram of the classifications for each of the 750 correlation functions in this study.

Relevant information from bins that were successfully fit according to the procedure outlined in Figure 4A was extracted for subsequent analysis. Figure 7 displays relaxation time and speed distributions from various oriented grains in this measurement. The relaxation time distribution in Figure 7A tends towards larger values of τ , likely due to the long relaxation times associated with particles within grains. For almost all fits, $\beta > 1$, indicating a compressed exponential form associated with ballistic or "hyperdiffusive" motion. Additionally, six heterodyne frequencies emerged to produce the speed distribution in Figure 7B, along with numerous additional heterodyne examples at different times and temperatures, which will be reported in a future publication. We postulate that the speeds observed in this experiment are due to the motion of individual grains. Indeed, the range of speeds recovered from this measurement (0.0093 Å/s $\leq u \leq 0.93$ Å/s) agrees well with the growth velocities reported for diblock copolymer grains from time-resolved depolarized light scattering experiments. However, we cannot exclude the possibility that these speeds stem from other dynamic features, including

dislocation movement, grain rotation, or a combination of several processes. A more in-depth analysis and interpretation of both the relaxation times and the speeds will be the subject of a future study.

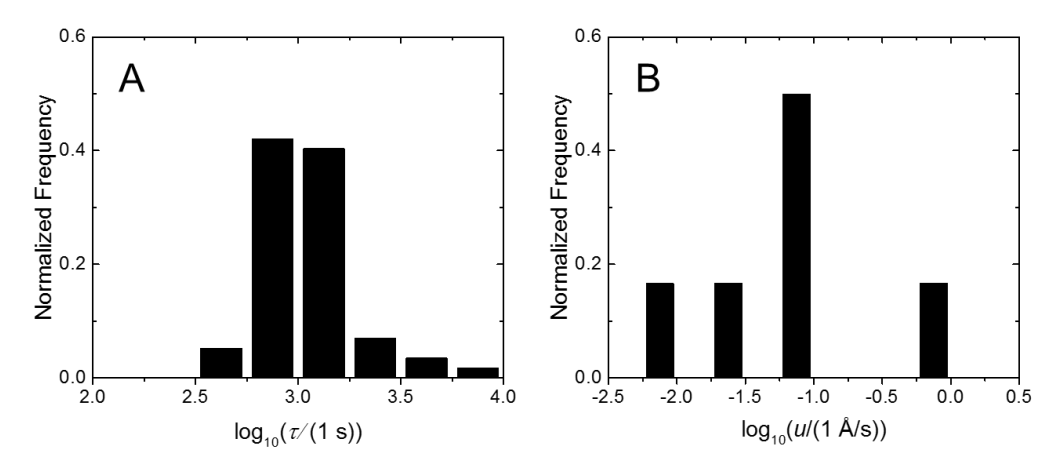


Figure 7: Normalized histogram plots reveal the complex dynamics of the ordered PS-PB system after annealing at 140 °C for approximately 7.5 h. The distribution of relaxation times in (A) was determined from Equations 4 and 10. Because the correlations were analyzed for dt < 800 s, we cannot definitively categorize $\tau > 10^4$ s and thus placed these data in the longest time bin. The distribution of speeds in (B) was determined from fits to Equations 10 and 11, and the dominant frequencies from FFT analysis. Note that the fitted parameters from bins which were categorized as either a single relaxation or a low frequency heterodyne (purple bins in Figure 4) are not included in either of these histograms.

Although this analytical method works well for the system studied here, there are some cases where it may not apply. For example, this analysis is unable to differentiate among multiple relaxation processes with nearly identical characteristic timescales. Additionally, there are limitations based on the grain size relative to the pixel size on the detector. Extremely large grains with strong Bragg peaks may saturate the detector and bleed into nearby pixels, complicating analysis. We expect these complications may arise as the bin size is reduced (or azimuthal resolution is increased) and/or detector saturation becomes prominent due to large ordered regions in the sample. Conversely, the presence of many overlapping small grains on a single pixel (or in this case, within a bin) may lead to analytical complexity through convolution

of multiple distinct timescales. Nevertheless, this high resolution mapping method and associated classification scheme represents a significant improvement over current averaging techniques and may prove useful for a variety of polycrystalline materials.

V. CONCLUSIONS

In this report a new analytical method is outlined for analysis of XPCS data from polycrystalline materials. This method was employed to investigate the dynamics of a BCC-forming diblock copolymer. A rotational mapping scheme was developed to balance high resolution with meaningful statistics for fitting. For the specific PS-PB diblock copolymer sample studied here, relevant theoretical equations were briefly described and a scheme was developed to implement these equations to fit the correlation functions from an exemplary set of XPCS data. The fitting procedure yielded relaxation time and speed distributions from distinct grains of micellar BCC structure within the bulk diblock copolymer sample. The relevant information uncovered by this method validate its execution and use and demonstrate that one XPCS measurement may yield a plethora of dynamic data with the proper analytical tools.

ACKOWLEDGEMENTS

Support for this work was provided by the National Science Foundation under Grants DMR-1104368, CHE-1608115, and DMR-17017578. SAXS experiments in the supporting information were conducted at the Advanced Photon Source (APS). Use of the APS, an Office of Science User Facility operated for the U.S. Department of Energy (DOE) Office of Science by Argonne National Laboratory, was supported by the U.S. DOE under Contract No. DE-AC02-06CH11357.

REFERENCES

(1) Gutt, C.; Ghaderi, T.; Chamard, V.; Madsen, A.; Seydel, T.; Tolan, M.; Sprung, M.; Grübel, G.; Sinha, S. K. *Phys. Rev. Lett.* **2003**, *91*, 076104.

- (2) Srivastava, S.; Archer, L. A.; Narayanan, S. *Phys. Rev. Lett.* **2013**, *110*, 1–5.
- (3) Srivastava, S.; Agarwal, P.; Mangal, R.; Koch, D. L.; Narayanan, S.; Archer, L. A. *ACS Macro Lett.* **2015**, *4*, 1149–1153.
- (4) Ulbrandt, J. G.; Rainville, M. G.; Wagenbach, C.; Narayanan, S.; Sandy, A. R.; Zhou, H.; Ludwig, K. F.; Headrick, R. L. *Nat. Phys.* **2016**, *12*, 794–799.
- (5) Sanz, A.; Ezquerra, T. A.; Hernández, R.; Sprung, M.; Nogales, A. *J. Chem. Phys.* **2015**, *142*, 064904.
- (6) Patel, A. J.; Mochrie, S. G. J.; Narayanan, S.; Sandy, A.; Watanabe, H.; Balsara, N. P. *Macromolecules* **2010**, *43*, 1515–1523.
- (7) Jang, W.-S.; Koo, P.; Sykorsky, M.; Narayanan, S.; Sandy, A.; Mochrie, S. G. J. *Macromolecules* **2013**, *46*, 8628–8637.
- (8) Sutton, M.; Mochrie, S. G. J.; Greytak, T.; Nagler, S. E.; Berman, L. E.; Held, G. A.; Stephenson, G. B. *Nature* **1991**, *352*, 608–610.
- (9) Lumma, D.; Lurio, L. B.; Mochrie, S. G. J.; Sutton, M. Rev. Sci. Instrum. **2000**, 71, 3274–3289.
- (10) Falus, P.; Borthwick, M. A.; Mochrie, S. G. J. Rev. Sci. Instrum. 2004, 75, 4383–4400.
- (11) Leheny, R. L.; Rogers, M. C.; Chen, K.; Narayanan, S.; Harden, J. L. Curr. Opin. Colloid Interface Sci. 2015, 20, 261–271.
- (12) Chung, B.; Ramakrishnan, S.; Bandyopadhyay, R.; Liang, D.; Zukoski, C. F.; Harden, J. L.; Leheny, R. L. *Phys. Rev. Lett.* **2006**, *96*, 3–6.
- (13) Patel, A. J.; Narayanan, S.; Sandy, A.; Mochrie, S. G. J.; Garetz, B. A.; Watanabe, H.; Balsara, N. P. *Phys. Rev. Lett.* **2006**, *96*, 1–4.
- (14) Oparaji, O.; Narayanan, S.; Sandy, A.; Ramakrishnan, S.; Hallinan, D. *Macromolecules* **2018**, *51*, 2591–2603.
- (15) Hillmyer, M. A.; Bates, F. S. *Macromolecules* **1996**, *29*, 6994–7002.
- (16) Khandpur, A. K.; Förster, S.; Bates, F. S.; Hamley, I. W.; Ryan, A. J.; Bras, W.; Almdal, K.; Mortensen, K. *Macromolecules* **1995**, *28*, 8796–8806.
- (17) Sinha, S. K.; Jiang, Z.; Lurio, L. B. Adv. Mater. **2014**, 26, 7764–7785.
- (18) Pennicard, D.; Lange, S.; Smoljanin, S.; Hirsemann, H.; Graafsma, H.; Epple, M.; Zuvic, M.; Lampert, M. O.; Fritzsch, T.; Rothermund, M. *J. Phys. Conf. Ser.* **2013**, *425*.
- (19) Berne, B. J.; Pecora, R. *Dynamic Light Scattering with Applications to Chemistry, Biology, and Physics*; John Wiley & Sons, Inc.: New York, 1976.
- (20) Cipelletti, L.; Ramos, L.; Manley, S.; Pitard, E.; Weitz, D. A.; Pashkovski, E. E.; Johansson, M. *Faraday Discuss.* **2003**, *123*, 237–251.
- (21) Livet, F.; Bley, F.; Ehrburger-Dolle, F.; Morfin, I.; Geissler, E.; Sutton, M. *J. Synchrotron Radiat.* **2006**, *13*, 453–458.
- (22) Livet, F.; Bley, F.; Ehrburger-Dolle, F.; Morfin, I.; Geissler, E.; Sutton, M. *J. Appl. Crystallogr.* **2007**, *40*, 38–42.
- (23) Lhermitte, J. R. M.; Rogers, M. C.; Manet, S.; Sutton, M. Rev. Sci. Instrum. 2017, 88.
- (24) Lee, S.; Leighton, C.; Bates, F. S. Proc. Natl. Acad. Sci. U. S. A. 2014, 111, 17723–17731.
- (25) Gillard, T. M.; Lee, S.; Bates, F. S. *Proc. Natl. Acad. Sci.* **2016**, *113*, 5167–5172.
- (26) Schatzel, K. Quantum Opt. J. Eur. Opt. Soc. Part B 1990, 2, 287–305.
- (27) Cipelletti, L.; Weitz, D. A. Rev. Sci. Instrum. 1999, 70, 3214–3221.
- (28) Balsara, N. P.; Garetz, B. A.; Chang, M. Y.; Dai, H. J.; Newstein, M. C.; Goveas, J. L.; Krishnamoorti, R.; Rai, S. *Macromolecules* **1998**, *31*, 5309–5315.
- (29) Dai, H. J.; Balsara, N. P.; Garetz, B. A.; Newstein, M. C. Phys. Rev. Lett. **1996**, 77, 3677–

3680.